magnetochemistry

MDPI

Article

The Impact of Ho Addition on the Microstructural Features and Magnetic Performances of Sintered NdFeB Magnets

Xin-De Zhu [1,2], Wei-Ming Liu [3], Fei Wang [1], Zhao-Pu Xu [4], Qian Wang [1], Xiao-Qian Gu [4], Meng Li [4], Ya Jiang [2], Feng-Sheng Xue [2] and Mei Wang [1,*]

1 Key Laboratory for Liquid-Solid Structural Evolution and Processing of Materials Ministry of Education, Shandong University, Jinan 250061, China; zhuxinde@sdu.edu.cn (X.-D.Z.); hqwangfei@163.com (F.W.); qian.wang@sdu.edu.cn (Q.W.)
2 Ningbo Jianxin Chassis System Co., Ltd., Ningbo 315033, China; jiangya@jianxin.com (Y.J.); fengsheng.xue@jianxin.com (F.-S.X.)
3 Yantai Standard and Metrology Inspection and Testing Center, Yantai 264000, China; 13863842589@139.com
4 Yantai Zhenghai Magnetic Material Co., Ltd., Yantai 264006, China; xuzhaopu@zhmag.com (Z.-P.X.); guxiaoqian@zhmag.com (X.-Q.G.); limeng@zhmag.com (M.L.)
* Correspondence: wangmei@sdu.edu.cn

Abstract: Two NdFeB magnets with distinct compositions were fabricated via an identical process. One magnet was doped with 2.5 wt.% of Ho, whereas the other remained undoped. Subsequently, grain boundary diffusion was performed on both magnets using metallic Tb, adopting the same set of technological parameters. A comprehensive analysis was conducted on the magnetic properties, phase compositions, microstructures, and elemental distributions of these two magnets. The findings indicate that the incorporation of Ho enhances the utilization efficiency of Tb. As a result, the magnets can achieve higher coercivity across different temperatures, with only a minor reduction in remanence. During the sintering process of the Ho-doped magnet, fine precipitated particles of $Ho_2Fe_{14}B$ are generated inside the magnet. This phenomenon causes the refinement of the main grains of the magnet. The refined main grains facilitate the effective diffusion of Tb within the magnet, eliminating the formation of the anti-shell structure. Furthermore, when Ho substitutes for Nd, it leads to a more homogeneous distribution of the Nd-rich phase. Additionally, it increases the densification degree of the sintered NdFeB magnets. These effects contribute to a further enhancement of the magnets' coercivity.

Keywords: sintered NdFeB magnets; Ho; coercivity; grain boundary diffusion

check for updates

Academic Editor: Carlos J. Gómez García

Received: 14 March 2025
Revised: 7 April 2025
Accepted: 10 April 2025
Published: 14 April 2025

Citation: Zhu, X.-D.; Liu, W.-M.; Wang, F.; Xu, Z.-P.; Wang, Q.; Gu, X.-Q.; Li, M.; Jiang, Y.; Xue, F.-S.; Wang, M. The Impact of Ho Addition on the Microstructural Features and Magnetic Performances of Sintered NdFeB Magnets. *Magnetochemistry* **2025**, *11*, 32. https://doi.org/10.3390/magnetochemistry11040032

Copyright: © 2025 by the authors. Licensee MDPI, Basel, Switzerland. This article is an open access article distributed under the terms and conditions of the Creative Commons Attribution (CC BY) license (https://creativecommons.org/licenses/by/4.0/).

1. Introduction

As wind power generation, electric motors, new-energy vehicles, and other fields experience swift development, the need for high-performance NdFeB permanent magnets is growing at a fast pace [1–5]. Thus, enhancing the magnetic properties of NdFeB has emerged as the foremost technical hurdle. Given the matrix phase's anisotropy has a strong temperature dependence, the magnetic properties decline sharply at elevated temperatures [6]. It is thought that having a coercivity (Hcj) high enough at room temperature is essential to counterbalance the loss of magnetic properties at high temperatures.

Based on the main coercivity mechanism of NdFeB magnets, the methods for enhancing the magnets' coercivity mainly involve optimizing the magnets' composition and processing technology. In industrial production, introducing heavy rare-earth elements like Tb and Dy is a viable way to notably boost coercivity. The grain boundary diffusion technology, a major innovation in the NdFeB magnet field in the 21st century, improves

the intrinsic magnetic properties and refines the grain boundary structure. It does this by introducing the diffusing agent into the NdFeB magnet along the grain boundaries, thereby decreasing the usage of heavy rare-earth elements while increasing the magnet's coercivity [7,8]. Nevertheless, in recent years, the surging demand for high-coercivity Nd-FeB magnets has caused the prices of heavy rare-earth elements to keep rising. Currently, the key development trends are to further minimize the consumption of heavy rare-earth elements, make efficient use of diffusing agents, and continuously lower material costs.

When aiming to maintain the performance of sintered NdFeB magnets, substituting the costly rare-earth elements Pr, Nd, Dy, and Tb, either partially or entirely, with more affordable ones like Ce [9,10], Gd [11], and Y [12] holds significant practical value. This substitution not only cuts down production costs but also promotes the balanced exploitation of rare-earth resources. Holmium (Ho), being one of the heavy rare-earth elements, is capable of forming the $RE_2Fe_{14}B$ compound. Despite the relatively low saturation magnetization polarization Js of $Ho_2Fe_{14}B$, which stands at 0.81 T, its high anisotropy field Ha = 75 kOe implies that Ho has the potential to enhance the performance of RE-Fe-B magnets [13], particularly those lacking critical rare-earth elements. Multiple research efforts have been conducted, and the findings suggest that incorporating the Ho element into a RE-Fe-B magnet can positively impact both coercivity enhancement and thermal stability [14–18]. The increase in coercivity is related to the microstructural characteristics. Nevertheless, the specific way in which the microstructure leads to the growth of coercivity is intricate and remains incompletely understood.

Consequently, the objective of this research was to examine the impacts of introducing metallic Ho into the raw materials before the sintering process. The goal was to realize a more significant elevation in intrinsic coercivity while maintaining a stable consumption level of heavy rare earths. Subsequently, a comprehensive study was carried out on the concomitant alterations in the magnetic properties, microstructure, and elemental composition distribution of the Tb-diffused magnets.

2. Materials and Methods

Sintered NdFeB magnets labeled as A and B, which possessed distinct compositions (as presented in Table 1), were manufactured through a series of processes. These processes included fully automatic scale casting. Then, the obtained strip-cast alloys were subjected to a hydrogen decrepitation process. Subsequently, jet milling and ball milling were carried out in sequence in a nitrogen atmosphere. The resulting powder was automatically molded, followed by continuous sintering at 1050 °C and subsequent double tempering treatment. The double tempering was carried out at 900 °C and 500 °C for 5 h respectively, in a mixed gas environment of N_2, Ar, and H_2, where the base pressure was less than 10^{-3} Pa. This manufacturing approach is known as the oxygen-free process technology [19]. In order to eliminate the impact of factors such as powder particle size variations and other process variables on the final analysis outcomes, the two types of magnets in this research were sintered with identical process parameters during the jet milling and ball milling stages. Specifically, they had an average particle size of roughly 4–5 μm, and other preparation process parameters were also kept consistent.

Table 1. Compositions (wt.%) of the original samples (A and B) of the NdFeB magnets.

Composition (wt.%)	Ho	Co	Nd	Fe	B	Ga	Cu
A	0	1.5	28	69.2	1.0	0.1	0.1
B	2.5	2.5	28.5	65.1	1.0	0.1	0.1

The obtained sintered NdFeB magnets, which were cylindrical in shape with dimensions of ϕ10 mm × 10 mm and had their preferred magnetization direction along the cylinder's axis, were chosen as the initial magnets for the Tb diffusion experiment. The technical parameters for Tb grain boundary diffusion were the same for both magnets. A self-designed three-dimensional magnetron sputtering device was employed. At room temperature, a Tb metal film was deposited on both the top and bottom surfaces of the magnets perpendicular to the c-axis. Metallic Tb with a purity exceeding 99.9% was used as the diffusion source, and the vacuum in the sputtering chamber was maintained at a level better than 3×10^{-6} Pa. The weight gain ratio of the Tb metal was 0.8%. Subsequently, grain boundary diffusion was performed under high vacuum conditions at 900 °C for 10 h, and then annealing was carried out at 500 °C for 2 h. The magnets after Tb diffusion were named A-GBD and B-GBD, respectively. The initial magnets and the magnets after Tb diffusion were cut into small pieces with dimensions of 7 mm × 5 mm × 5 mm (c-axis direction). Subsequently, these small pieces were cleaned and polished to facilitate the examination.

The magnetic properties of the magnets both prior to and following diffusion were measured at 20 °C, 90 °C, and 140 °C. This was accomplished using a hysteresigraph (NIM-10000H, Beijing, China). For the investigation of the surface phases of the magnets before and after diffusion, a X-ray diffraction (XRD, D/Max2550VB, Tokyo, Japan) instrument, which utilized Cu K-beta radiation, was employed. The microstructural observation was carried out with a field-emission scanning electron microscope (FESEM, JSM-7800F, Tokyo, Japan). The area distribution of the main elements was ascertained by a electron probe microanalyzer (EPMA, JXA-8530F Plus, Tokyo, Japan).

3. Results and Discussion

3.1. Magnetic Properties and Temperature Stability

Figure 1 demonstrates the demagnetization curves of the two types of magnets at 20 °C before and after the diffusion treatment. The magnetic properties of the magnets are listed in Table 2. Compared with magnet A (with a coercivity of 11.10 kOe), magnet B exhibits a higher coercivity (12.54 kOe), and due to the addition of Ho, the remanence decreases from 14.82 kGs to 13.66 kGs. This indicates that the addition of Ho can improve the coercivity of the magnet, but there will be a certain loss of remanence simultaneously, which is similar to the cases of adding Tb and Dy [8]. After the grain boundary diffusion treatment of Tb with the same weight gain ratio, the coercivity of magnet A-GBD increases from 11.10 kOe to 23.82 kOe, while the coercivity of magnet B-GBD increases from 12.54 kOe to 26.61 kOe. As shown in Figure 1a, it is evident that the B-GBD magnet has a higher coercivity and a larger increment in coercivity compared with the A-GBD magnet.

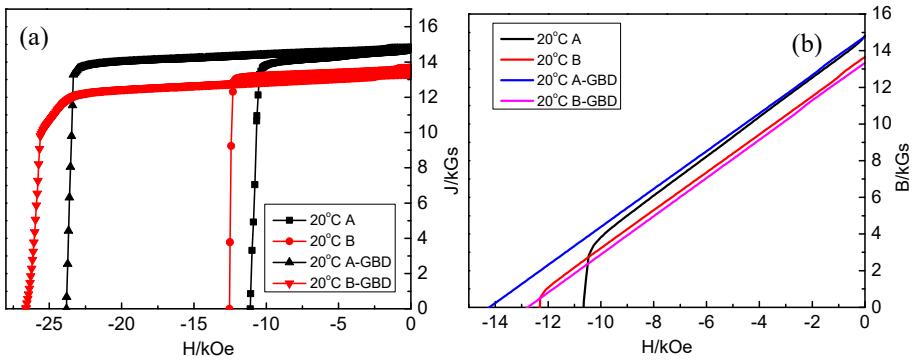


Figure 1. Demagnetization J-H (**a**) and B-H (**b**) curves of the magnets after Tb diffusion at 20 °C.

Table 2. Magnetic properties at different temperatures of the magnets before and after Tb diffusion.

Sample	Temperature (°C)	Br (kGs)	α (%/°C)	Hcj (kOe)	β (%/°C)	(BH)max (MGOe)
A	20	14.82		11.10		50.15
B	20	13.66		12.54		44.50
A-GBD	20	14.76		23.82		52.46
	140	11.91	−0.16	6.33	−0.61	32.87
B-GBD	20	13.34		26.61		42.47
	140	11.68	−0.10	11.69	−0.47	31.84

The linear B-H curve is a very important characteristic that enables the magnets to be stable during operation. Under ideal conditions, it should be a straight line with a slope of 1. Figure 1b depicts the magnet remanence (Br) variations of the A and B magnets before and after Tb diffusion at 20 °C, reflecting the maximum magnetic energy product (BHmax) of the magnets. The B-H curves of the A-GBD and B-GBD magnets (blue line and magenta line) show a straight line, while the curves of the original magnets show a knee-like characteristic when the residual magnetism approaches zero, and the situation with magnet A is a bit more serious. A knee point appears on the B-H curve, indicating poor coercivity or squareness of the magnet, which is unfavorable to the stable operation of the magnet. This shows that the structure and density of the magnet are improved after the addition of Ho. In addition, the diffusion of Tb has a more obvious effect on the microstructure and density of the magnet. As shown in Table 2, after Tb diffusion, the corresponding maximum magnetic energy product (BH max) of magnet A at 20 °C increases from 50.15 MGOe to 52.46 MGOe, but that of magnet B shows a decrease from 44.50 MGOe to 42.47 MGOe. It can be deduced that the addition of Ho strengthens the magnetism reduction caused by Tb diffusion.

Figure 2 shows the demagnetization J-H (a) and B-H (b) curves of the magnets after Tb diffusion at 20 °C and 140 °C. The magnetic properties of the magnets are listed in Table 2. It can be found that both the coercivity and remanence of the A-GBD and B-GBD magnets decrease as the temperature increases, but the B-GBD magnet has higher coercivity than the A-GBD magnet at both 20 °C and 140 °C. However, the corresponding maximum magnetic energy product of the A-GBD magnet is higher than that of the B-GBD magnet. When the magnetic induction intensity B value is close to 0, a knee point appears on the B-H curve of the A-GBD magnet at 140 °C. However, the B-H curve of the B-GBD magnet at 140 °C does not show a knee point in the second quadrant, so it is more stable under working conditions.

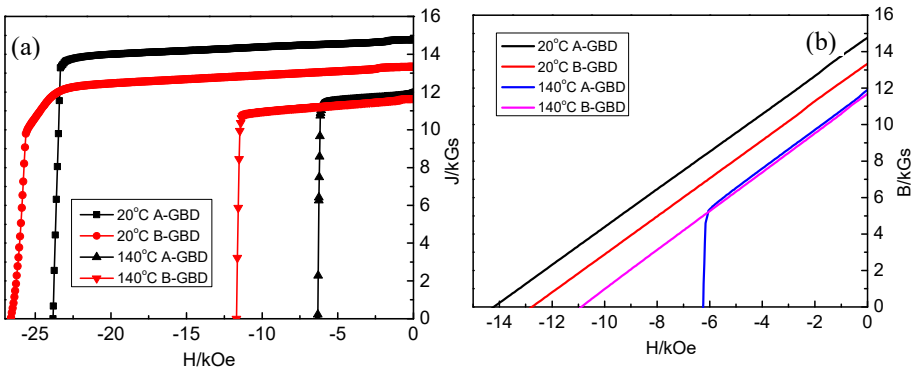


Figure 2. Demagnetization J-H (**a**) and B-H (**b**) curves of the magnets after Tb diffusion at 20 °C and 140 °C.

The remanence temperature coefficient (α) and the coercivity temperature coefficient (β) of magnets at 20–140 °C were calculated, respectively, and the results are listed in Table 2. The remanence temperature coefficient of the A-GBD magnet is −0.16%/°C at 20–140 °C, which is much larger than that of the B-GBD magnet (−0.10%/°C). This is probably caused by the formation of non-magnetic phases in the process of grain boundary diffusion. The coercivity temperature coefficient of the B-GBD magnet is −0.47%/°C at 20–140 °C, which is smaller than that of the A-GBD magnet (−0.61%/°C), indicating better coercivity thermal stability. This can be attributed to the optimized microstructure (this will be discussed in Section 3.2). In general, the B-GBD magnet exhibits better thermal stability than the A-GBD magnet.

Based on the above results, it can be inferred that the addition of Ho results in higher coercivity at different temperatures. The same phenomenon was also observed in the Tb and Dy diffusion experiments [8,20].

3.2. Microstructure and Elemental Distribution

Given that the coercivity of the NdFeB permanent magnets exhibits a high degree of sensitivity toward their microstructural features, particularly the grain boundary structure and chemical composition, the phase structure, microstructural morphology, and elemental distribution within these magnets were comprehensively investigated through XRD, FESEM, and EPMA analyses.

The XRD diffraction patterns of the four types of samples (A, A-GBD, B, and B-GBD) are shown in Figure 3. As can be seen from Figure 3a, the main diffraction peaks of the four samples appear at around 29° and 44°, respectively, corresponding to the (004) and (006) directions. Both of these are characteristic peaks of the Nd2Fe14B phase, which is the magnetic source of the magnet. The additional characteristic peaks (008) and (105) of NdFeB appear at approximately 60° and 39°. In the B and B-GBD samples, strong (008) and (105) peak signals can be observed, while in the A and A-GBD samples, the diffracted peak signals are rather weak, indicating that there are more defects in the latter. Nevertheless, the intensity values of (006) for the four types of samples are all higher than those of (105), which demonstrates that the c-axis orientation of the magnets was substantially preserved after diffusion, showing that all the magnets have good orientation.

The magnified patterns within the ranges of (b) 28–32° and (c) 42–47° are presented in Figure 3b,c. From Figure 3b, it is evident that samples A and A- GBD exhibit a prominent diffraction peak at around 31°. By referring to the data in reference [21], it is hypothesized that this peak corresponds to the (101) plane of hexagonal RE_2O_3 (h-RE_2O_3). When compared with the two original magnets, the (006) diffraction peaks of the magnets following the diffusion treatment display a slight shift towards larger angles (Figure 3c). According to the Bragg equation $2d\sin\theta = n\lambda$ [22], the shift of the diffraction peak toward a higher angle implies a reduction in the crystal plane spacing. This phenomenon is attributed to the partial substitution of Nd elements by Tb elements in the epitaxial layer of the main phase, thereby forming the $(Tb, Nd)_2Fe_{14}B$ phases. Given that the atomic radius of Tb (0.177 nm) is smaller than that of Nd (0.181 nm), the lattice constant and crystal plane spacing decrease after the substitution, consequently causing the diffraction peak shift. As depicted in Figure 3c, a satellite peak emerges adjacent to the (006) diffraction peaks of the B and B-GBD magnets. This peak corresponds to the same crystal plane of $Ho_2Fe_{14}B$, signifying that the addition of Ho as a raw material gives rise to a new 2:14:1 phase. Additionally, the signal of $Ho_2Fe_{14}B$ can also be detected at the (004) position of the B and B-GBD magnets, which leads to the shift of the (004) peak toward the lower-angle direction.

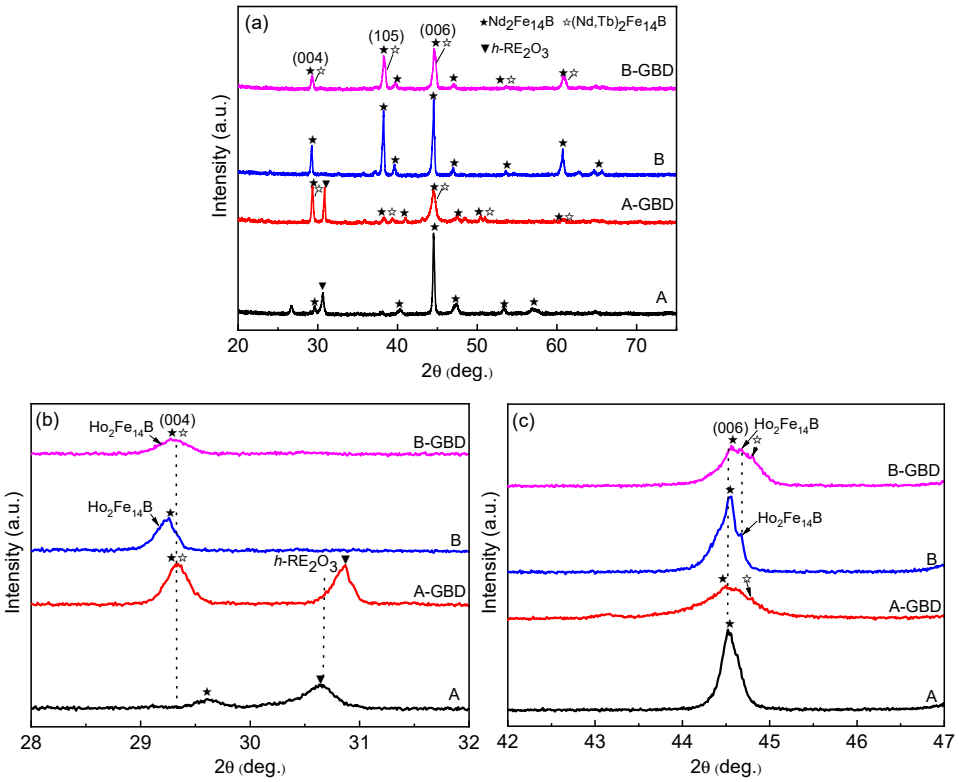


Figure 3. (**a**) XRD diffraction patterns of A, A-GBD, B, and B-GBD magnets and the enlarged patterns in the ranges of (**b**) 28–32° and (**c**) 42–47°. The XRD patterns were detected at the surface perpendicular to the c-axis.

Figure 4 illustrates the cross-sectional BSE-SEM images of the sintered magnets and the diffused magnets at varying depths (specifically, 50 μm, 100 μm, and 300 μm beneath the diffusion surfaces). Figure 4(a0) reveals that the grain size of the Ho-free sintered magnet is relatively coarse and inconsistent. There are numerous abnormally large grains, and the distribution of the grain boundaries appears indistinct. Upon the addition of Ho, as is evident from Figure 4(b0), the grain size of the main phase diminishes. The main grains are uniform in size, and their boundaries are distinct, resulting in a rather ideal microstructure. Figure 4c displays the line scanning results of magnet B. As shown in Figure 4c, Ho is distributed both within the grains of the main phase and at the grain boundaries. In magnet B, the concentration of Ho inside the matrix grains is lower than that at the grain boundaries.

Compared with the sintered magnets, continuous grain boundaries, as expected, are formed in the A-GBD and B-GBD magnets after Tb diffusion (Figure 4). Two types of grain boundaries with different contrasts can be clearly observed due to their different chemical compositions. It has been reported that Tb atoms can diffuse into the main phase lattice, resulting in the formation of a $(Nd,Tb)_2Fe_{14}B$ shell [8,23]. This core–shell structure is a typical structure in heavy rare-earth diffused magnets. In the back-scattered mode of a scanning electron microscope, the atomic number of the heavy rare-earth-rich shell is larger than that of the $Nd_2Fe_{14}B$ core, so the contrast is lighter. At depths of 50 μm and 100 μm, it can be clearly seen that there is a distinct interface between the Tb-rich shell and the $Nd_2Fe_{14}B$ core in the two diffused magnets (the boundary between the two regions is marked with a black dashed line in Figure 4(a1,a2,b1,b2)). The A-GBD magnet has thicker Tb-rich shells than the B-GBD magnet at 50 μm and 100 μm, implying there is an enrichment of Tb in the surface layer of the magnet. Excessively thick Tb-rich shells will consume more Tb, and it is not beneficial to the deep diffusion of Tb into the magnet. At a depth of 300 μm,

no obvious Tb-rich shell can be observed in either the A-GBD magnet or the B-GBD magnet, indicating that the concentration of Tb here is relatively low (Figure 4(a3,b3)).

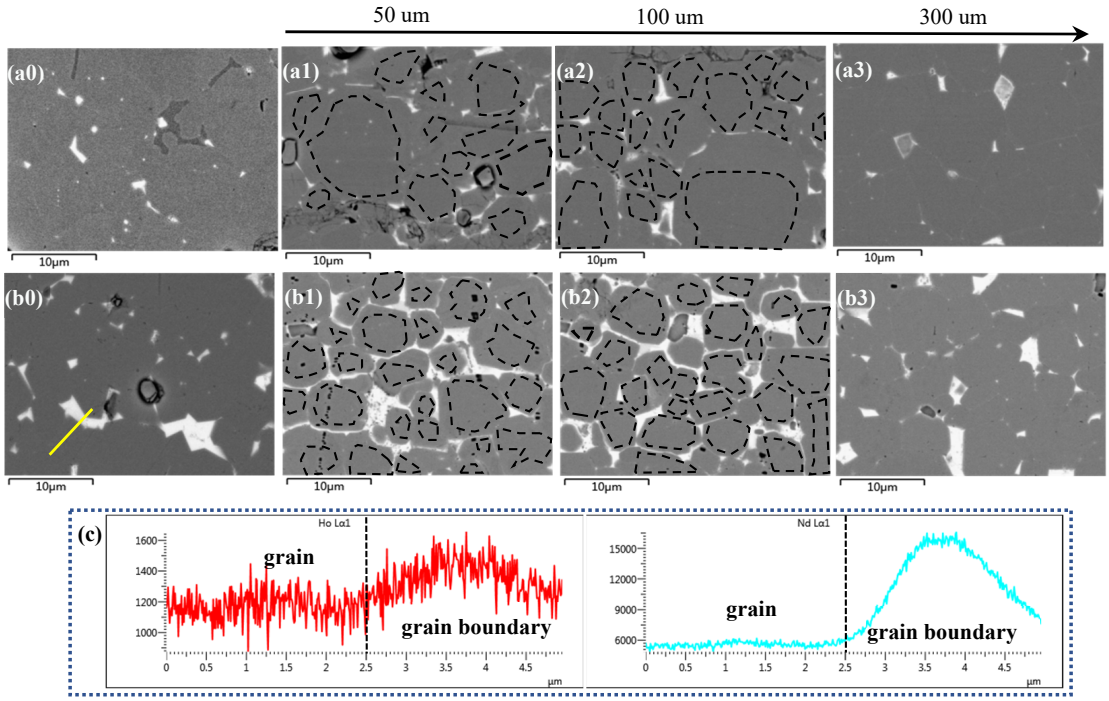


Figure 4. Back-scattered electron SEM images of A (**a0**), B (**b0**) sintered magnet, and A-GBD (**a1**,**a2**,**a3**) and B-GBD (**b1**,**b2**,**b3**) magnets at different diffusion depths (**a1**,**b1**): 50 μm, (**a2**,**b2**): 100 μm, and (**a3**,**b3**): 300 μm. The main phase core is within the dashed circle. (**c**) Line scanning profiles along the yellow line in (**b0**).

Figure 5 depicts the EPMA images of the cross-sections of the A-GBD and B-GBD magnets at a depth of 0~300 μm. By comparing the two types of diffused magnets, it can be clearly observed that the microstructure of the B-GBD magnet is finer than that of the A-GBD magnet. This indicates that the addition of Ho leads to the refinement of the magnet's grains. Figure 5(a1,b1) show that the concentration of Tb decreases as the diffusion depth increases in both magnets, and the Tb distribution of the B-GBD magnet is more uniform and dispersed from the surface to a depth of 300 μm in comparison with that of the A-GBD magnet. At the same Tb weight gain ratio, there are more Tb elements concentrated near the surface of the A-GBD magnet than those near the surface of the B-GBD magnet, indicating the Tb diffusion in the B-GBD magnet is relatively more sufficient. Three types of microstructures located in sequenced zones are marked with I, II, and III in Figure 5(a1,b1), and their microstructures at higher magnification are exhibited in Figure 6. The concentration of Nd shows a nearly opposite variation to that of Tb (Figure 5(a2,b2)). A significant decrease in Nd enrichment near the surface of the magnets can be clearly observed in both types of magnets, as shown in Figure 5(a2,b2).

BSE images and EPMA element mappings for the diffused magnets are shown in Figure 6. At a depth of 50 μm, a cloud-like Tb-rich structure can be observed in the A-GBD magnet, corresponding to the structure of Type I in Figure 5(a1). After Tb diffusion, Tb occupies most areas near the surface and forms an anti-shell structure of the main grain of the NdFeB magnet, which has been reported by other researchers [24]. In contrast, Figure 6(b1) shows that the B-GBD magnet formed a fairly thick Tb-rich network structure around the Tb-poor cores at a depth of 50 μm. This structure corresponds to Type II in Figure 5(b1). The same network structure can also be observed at a depth of 100 μm in the A-GBD magnet (Figure 5(a2)). This phenomenon is attributed to the relatively high

concentration of Tb at the grain boundaries. It causes a large amount of Tb to enter the 2:14:1 phase, forming a thick Tb-rich shell layer around the grains. As depicted in Figure 6(b2), a thin Tb-rich network, which corresponds to the Type-III structure in Figure 5(b1), can be observed in the B-GBD magnet at a depth of 100 μm. This indicates that, due to the low Tb content at the grain boundaries, only a small amount of Tb atoms enter the main-phase grains, thus forming a thin Tb-rich shell layer. This is in line with Fick's laws of diffusion.

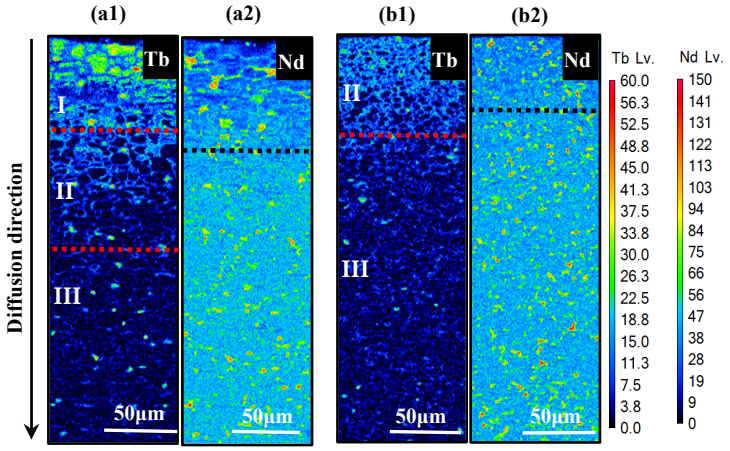


Figure 5. Cross-sectional EPMA images of A-GBD (**a1**,**a2**) and B-GBD (**b1**,**b2**) magnets at 0~300 μm (Type I: anti-shell; Type II: core-thick shell; Type III: core-shell).

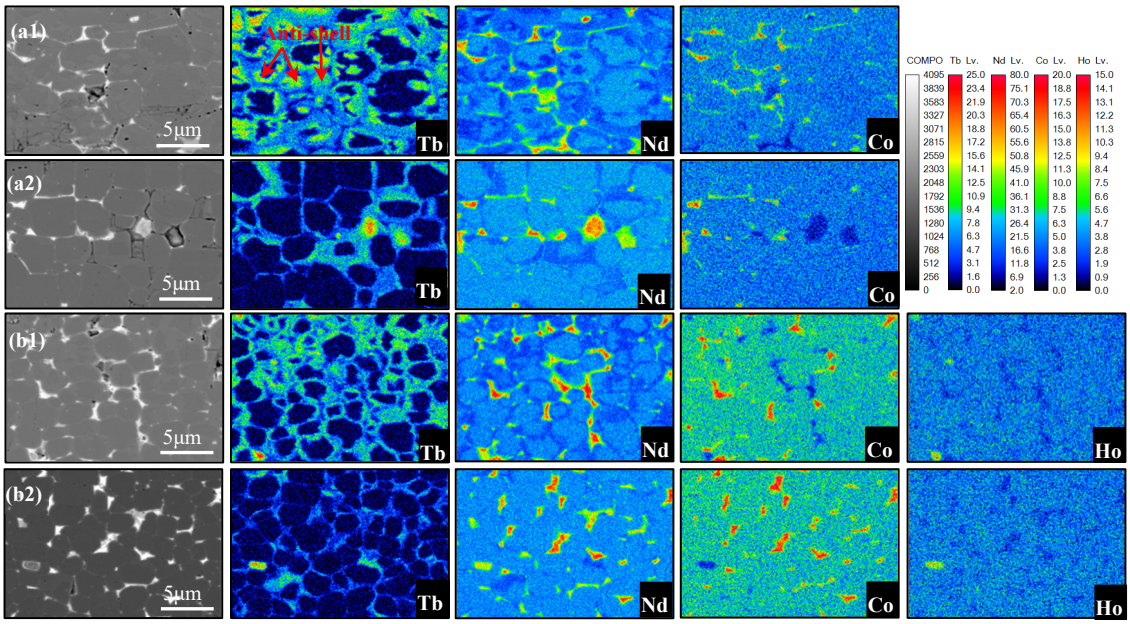


Figure 6. BSE images and EPMA element scan images of A-GBD (**a1**,**a2**) and B-GBD (**b1**,**b2**) magnets at different diffusion depths: (**a1**,**b1**): 50 μm; (**a2**,**b2**): 100 μm.

Given that the anisotropy field of $Tb_2Fe_{14}B$ surpasses that of $Nd_2Fe_{14}B$ [6], the existence of the Tb-rich shell intensifies the magnetic hardening at the interface. This, in turn, restrains the nucleation of reverse domains, thus augmenting the coercivity. Nevertheless, when an excessive number of Tb atoms diffuse into the main-phase lattice, it causes the formation of an overly thick Tb-rich shell and an anti-shell structure, as illustrated in Figure 7.

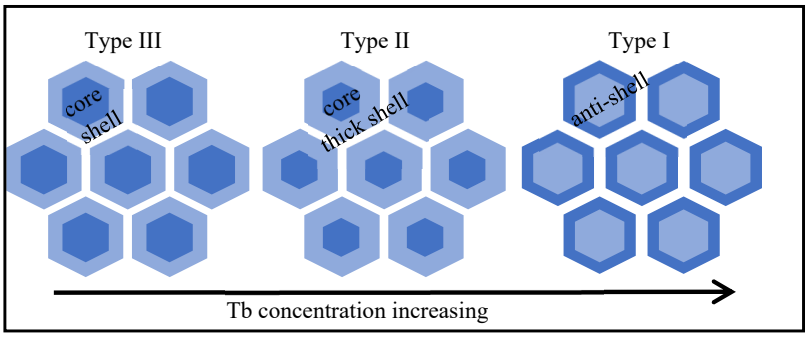


Figure 7. Three types of structures (Type I: anti-shell; Type II: core-thick shell; Type III: core-shell) with different Tb concentrations.

As described previously, near the diffusion source, the Tb concentration in the shell of the main-phase grains of the A-GBD magnet is notably higher than that in the shell of the main-phase grains of the B-GBD magnet. In the A-GBD magnet, Tb is distinctly concentrated in the surface layer (Figure 5). Figure 6 indicates that an anti-shell structure is formed at a depth of 50 μm in the A-GBD magnet, while the B-GBD magnet does not exhibit such a structure at the same depth. At a depth of 100 μm, compared with the B- GBD magnet, the A-GBD magnet develops a thicker Tb-rich shell (Figure 6). Based on the large-scale micromagnetic simulation conducted by Ohkubo et al. [25], a Tb-rich shell with a thickness of 15 nm is adequate to boost the coercivity. An overly thick shell not only fails to further enhance the coercivity but also results in a waste of Tb resources. Additionally, the anti-shell structure can produce a substantial stray field, which will expedite the magnetization reversal of the entire magnet, thus exerting a negative impact on the coercivity of the diffused magnets. This finding is in line with the magnetic property results presented in Section 3.1.

As depicted in Figure 6(a1), by comparing the back-scattered electron (BSE) images with the corresponding EPMA mapping of Nd, it can be observed that at a depth of 50 μm, Nd is distributed along the grain boundaries in the A-GBD magnet. In the anti-shell structure, the concentrations of Nd and Tb exhibit a complementary relationship. In areas where the Tb concentration is high, the Nd concentration is low. This confirms that the formation of the anti-shell structure is attributed to a large number of Tb atoms substituting for Nd and entering the lattice of the main phase. At depths of both 50 μm and 100 μm, the distribution of Nd elements in the B-GBD magnet is more uniform and dispersed compared with that in the A-GBD magnet. This is because the added Ho dissolves in the main phase, replaces part of the Nd metal, and forms the $Ho_2Fe_{14}B$ phase (as shown in Figure 3), thereby increasing the melting point of the alloy. Under the same strip-casting process, increasing the degree of undercooling of the molten solution can effectively suppress the formation of the α-Fe phase. At the same time, the increase in undercooling promotes the growth of columnar crystals, making the distribution of the Nd-rich phase more uniform.

Combining the above results of XRD analysis with those of Figure 4c, it can be speculated that during the sintering process of Nd-Fe-B magnets, fine precipitated particles of $Ho_2Fe_{14}B$ with high melting points are distributed either within the main phase grains or at the grain boundaries. These $Ho_2Fe_{14}B$ particles inhibit the growth of main phase grains during sintering and pin the magnetic domain walls, thus refining the grains. As shown in Figure 6(b1,b2), the concentration of Ho within the matrix grains is higher than that at the grain boundaries in the B-GBD magnet, which is consistent with the results of sample B before diffusion (Figure 4c). Ho distributed at the grain boundaries can increase the quantity of the rare-earth-rich phase at the grain boundaries, effectively improve the wettability of the grain boundary phase, eliminate the direct contact between grains, reduce

the proportion of intergranular fracture, decrease the surface defects of the grains, improve the compactness of the magnet, and endow it with excellent comprehensive properties. Therefore, as shown in Figures 5 and 6, we can observe that the microstructure of the magnet with the addition of Ho is finer and denser, which, in turn, enhances the coercivity of the magnet.

The addition of Ho can enhance the coercivity but decrease the Curie temperature [6]. It has been reported that Co can replace Fe in the lattice of the main phase to form Nd2Co14B, which can significantly increase the Curie temperature of the main phase. Some research indicates that substituting 1 at.% of Fe in the magnet's composition with Co can increase the magnet's Tc by approximately 11 K [26]. Therefore, 2.5 wt.% of Co was added to the B magnet, while the Co content in the A magnet is 1.5 wt.%. As shown in Figure 6(b1,b2), Co tends to distribute at the grain boundaries in the A-GBD and B-GBD magnets, and the distribution of Co elements in the B-GBD magnet is more dispersed than that in the A-GBD magnet, which is similar to the distribution of Nd.

4. Conclusions

When 2.5 wt.% Ho is added to NdFeB magnets, fine precipitated particles of $Ho_2Fe_{14}B$ are formed inside the magnets during the sintering process. This results in the refinement of the main grains of the magnets. By minimizing the micro-structural defects and the stray fields generated by adjacent grains, this grain refinement plays a crucial role in boosting the coercivity. Moreover, on the surface of the diffused magnet, when an excessive quantity of Tb atoms diffuse into the main-phase lattice, it causes the formation of an overly thick Tb-rich shell and an anti-shell structure in the Ho-free magnet. Nevertheless, with the incorporation of Ho, the refined main grains allow Tb to diffuse effectively within the magnet, getting rid of the anti-shell structure. This not only further heightens the coercivity but also cuts down the consumption of Tb. Additionally, the replacement of Nd with Ho leads to a more uniform distribution of the Nd-rich phase and raises the densification level of the sintered NdFeB magnets. As a result, the coercivity of the magnets is further improved.

Author Contributions: Conceptualization, X.-D.Z., W.-M.L., F.W., Z.-P.X., Q.W., X.-Q.G., M.L., Y.J., F.-S.X. and M.W.; investigation, X.-D.Z., W.-M.L., F.W., Z.-P.X., Q.W., X.-Q.G., M.L., Y.J., F.-S.X. and M.W.; resources, Z.-P.X., X.-Q.G. and M.L.; writing—original draft preparation, M.W.; writing—review and editing, X.-D.Z., F.W. and Q.W.; supervision, Z.-P.X. and X.-D.Z.; project administration, Z.-P.X. and X.-D.Z.; funding acquisition, Z.-P.X. and X.-D.Z. All authors have read and agreed to the published version of the manuscript.

Funding: This research was funded by the Key Research and Development Program of Shandong Province (grant numbers: 2021CXGC010310 and 2024CXGC010319), the Shandong Province Science and Technology Small- and Medium-Sized Enterprise Innovation Ability Enhancement Project (grant numbers: 2023TSGC0287 and 2024TSGC0519).

Data Availability Statement: Data is contained within the article.

Conflicts of Interest: Zhao-Pu Xu, Xiao-Qian Gu, Meng Li, Ya Jiang, Feng-Sheng Xue, Xin-De Zhu are employed by "YanTai Zhenghai Magnetic Material Co., Ltd." and "Ningbo Jianxin Chassis System Co., Ltd." The remaining authors declare that the research was conducted in the absence of any commercial or financial relationships that could be construed as a potential conflict of interest.

References

1. Gutfleisch, O.; Willard, M.A.; Bruck, E.; Chen, C.H.; Sankar, S.G.; Liu, J.P. Magnetic materials and devices for the 21st century: Stronger, Lighter, and More Energy Efficient. *Adv. Mater.* **2011**, *23*, 821–842. [CrossRef] [PubMed]
2. Sugimoto, S. Current status and recent topics of rare-earth permanent magnets. *J. Phys. D Appl. Phys.* **2011**, *44*, 110–118. [CrossRef]
3. Deng, X.; Ge, J. Global wind power development leads to high demand for neodymium praseodymium (NdPr): A scenario analysis based on market and technology development from 2019 to 2040. *J. Clean. Prod.* **2020**, *277*, 123299. [CrossRef]
4. Liu, T.; Li, R.Y.; Zhou, L.; Shi, X.N.; Wei, Z.Y.; Ren, M.; Guo, X.Y. Progress of coercivity enhancement in sintered NdFeB magnets. *J. Chin. Soc. Rare Earths* **2024**, *1*, 1. (In Chinese)
5. Li, J.N.; Sepehri-Amin, H.; Sasaki, T.; Ohkubo, T.; Hono, K. Most frequent-ly asked questions about the coercivit y of Nd-Fe-B permanent magnets. *Sci. Technol. Adv. Mater.* **2021**, *22*, 386. [CrossRef] [PubMed]
6. Satoshi, H.; Yutaka, M.; Hitoshi, Y.; Setsuo, F.; Masato, S.; Hiroshi, Y. Magnetization and magnetic anisotropy of R2Fe14B measured on single crystals. *J. Appl. Phys.* **1986**, *59*, 873.
7. Nakamura, H.; Hirota, K.; Shimao, M. Magnetic properties of extremely small Nd-Fe-B sintered magnets. *IEEE Trans. Magn.* **2005**, *41*, 3844. [CrossRef]
8. Zhu, X.D.; Wang, M.; Yu, Y.J.; Wang, Q.; Wang, F.; Wang, P.F.; Jia, B.; Wang, C.; Zhou, B. Coercivity enhancement of sintered Nd-Pr-Fe-B magnets by cost-Effective grain boundary diffusion of Dy/Tb films. *Crystals* **2023**, *13*, 1516. [CrossRef]
9. Shao, X.H.; Zhou, X.Q.; Liang, S.H.; Yang, C.; Que, Y.S.; Guo, B.; Bao, H.P.; Tang, G.C.; Yan, X.L.; Bao, J.S.; et al. Research progress and prospects of Ce-containing NdFeB permanent magnets. *J. Alloys Compd.* **2025**, *1014*, 178567. [CrossRef]
10. Chen, B.; Ju, J.Y.; Yin, W.Z.; Tang, X.; Chen, R.J.; Yan, A.R.; Hou, L.Q.; Du, Y.Y. Coercivity enhancement of Ce-containing hot-deformed magnets by grain boundary diffusion of DyF_3. *J. Rare Earths* **2022**, *40*, 289–295. [CrossRef]
11. Zhou, B.; Liu, Y.T.; Li, S.M.; Fan, W.B.; Liao, X.F.; He, J.Y.; Yu, H.Y.; Liu, Z.W. Phase precipitation and magnetic properties of melt-spun ternary $Gd_2Fe_{14}B$ alloy and advantages of gadolinium substitution in $Y_2Fe_{14}B$ alloy. *J. Rare Earths* **2023**, *41*, 1058–1067. [CrossRef]
12. Liu, Y.T.; Fan, Y.W.; Gleb, M.; Liao, X.F.; Zhang, J.S.; Yu, H.Y.; Liu, Z.W. Fundamental properties of melt-spun stoichiometric $Y_2Fe_{14}B$ alloy and the advantages of Nd substitution. *J. Magn. Magn. Mater.* **2021**, *529*, 167898. [CrossRef]
13. Brown, D.N.; Lau, D.; Chen, Z. Substitution of Nd with other rare earth elements in melt spun $Nd_2Fe_{14}B$ magnets. *AIP Adv.* **2016**, *6*, 056019. [CrossRef]
14. Ramesh, R.; Thomas, G.; Ma, B.M. Improvement in intrinsic-coercivity of sintered Fe-Nd-B magnets by the introduction of non-magnetic dispersoids. *Acta Metall.* **1989**, *37*, 1421. [CrossRef]
15. Liang, L.P.; Ma, T.Y.; Wu, C.; Zhang, P.; Liu, X.L.; Yan, M. Coercivity enhancement of Dy-free Nd-Fe-B sintered magnets by intergranular adding Ho63.4Fe36.6 alloy. *J. Magn. Magn. Mater.* **2016**, *397*, 139. [CrossRef]
16. Di, J.H.; Guo, S.; Chen, L.; Yi, P.P.; Ding, G.F.; Chen, K.; Li, M.; Lee, D.; Yan, A. Improved corrosion resistance and thermal stability of sintered Nd-Fe-B magnets with holmium substitution. *J. Rare Earths* **2018**, *36*, 826–831. [CrossRef]
17. Li, S.M.; Zhou, B.; Liao, X.F.; Yu, H.Y.; Liu, Z.W. Phase precipitation and properties of melt-spun Ho-Fe-B alloys prepared by direct quenching and over-quenching followed by heat treatment. *Intermetallics* **2022**, *150*, 107688. [CrossRef]
18. Wang, H.Z.; Li, Z.J.; Liu, Z.; Yan, Y.; Zhi, P.Y. Effects of Ho nanopowders intergranular addition on microstructure and properties of sintered Nd-Fe-B. *J. Nanopart. Res.* **2021**, *23*, 237. [CrossRef]
19. Xie, H.Z. *Theory and Practice of NdFeB Oxygen Free Process Technology*, 1st ed.; Metallurgical Industry Press: Beijing, China, 2018; p. 21. (In Chinese)
20. Zhou, T.J.; Chen, J.; Wang, Q.R.; Pan, W.M.; Huang, Q.F.; Liu, R.H.; Li, M.F.; Xie, G.Q. Super-high coercivity NdFeB magnet fabricated with double Tb-rich/lean shells by double alloy method and grain boundary diffusion. *J. Alloys Compd.* **2023**, *937*, 168368. [CrossRef]
21. He, J.Y.; Yu, Z.G.; Cao, J.L.; Song, W.Y.; Xu, K.; Fan, W.B.; Yu, H.Y.; Zhong, X.C.; Mao, H.Y.; Mao, C.Y.; et al. Rationally selecting the chemical composition of the Nd-Fe-B magnet for high-efficiency grain boundary diffusion of heavy rare earths. *J. Mater. Chem. C* **2022**, *10*, 2080. [CrossRef]
22. Pope, C.G. X-Ray Diffraction and the Bragg Equation. *J. Chem. Edu.* **1997**, *74*, 129–131. [CrossRef]
23. Hirota, K.; Nakamura, H.; Minowa, T.; Honshima, M. Coercivity Enhancement by the Grain Boundary Diffusion Process to Nd-Fe-B Sintered Magnets. *IEEE Trans. Magn.* **2006**, *42*, 10. [CrossRef]
24. Li, W.D.; Zhang, Q.K.; Zhu, Q.H.; So, X.; Li, C.X.; Yang, J.; Zheng, B.Z.; Mao, S.D.; Song, Z.L. Formation of anti-shell/core structure of heavy rare earth elements (Tb, Dy) in sintered Nd-Fe-B magnet after grain boundary diffusion process. *Scr. Mater.* **2019**, *163*, 40–43. [CrossRef]

25. Oikawa, T.; Yokota, H.; Ohkubo, T.; Hono, K. Large-scale micromagnetic simulation of Nd-Fe-B sintered magnets with Dy-rich shell structures. *AIP Adv.* **2016**, *6*, 056006. [CrossRef]
26. Pandian, S.; Chandrasekaran, V.; Markandeyulu, G.; Iyer, K.J.L.; Rama Rao, K.V.S. Effect of Co, Dy and Ga on the magnetic properties and the microstructure of powder metallurgically processed Nd-Fe-B magnets. *J. Alloys Compd.* **2004**, *364*, 295–303. [CrossRef]

Disclaimer/Publisher's Note: The statements, opinions and data contained in all publications are solely those of the individual author(s) and contributor(s) and not of MDPI and/or the editor(s). MDPI and/or the editor(s) disclaim responsibility for any injury to people or property resulting from any ideas, methods, instructions or products referred to in the content.